



Vertical Airborne Wind Energy Farms with High Power Density per Ground Area based on Multi-Aircraft Systems

Jochem De Schutter^{a,*}, Jakob Harzer^a, Moritz Diehl^{a,b}

^a Department of Microsystems Engineering (IMTEK), University of Freiburg, Freiburg, 79110, Germany

^b Department of Mathematics, University of Freiburg, Freiburg, 79110, Germany

ARTICLE INFO

Article history:

Received 15 May 2023

Accepted 8 June 2023

Available online 22 June 2023

Recommended by Prof. T Parisini

Keywords:

Renewable energy

Optimal control

Airborne wind energy

ABSTRACT

This paper proposes and simulates vertical airborne wind energy (AWE) farms based on multi-aircraft systems with high power density (PD) per ground area. These farms consist of many independently ground located systems that are flying at the same inclination angle, but with different tether lengths, such that all aircraft fly in a large planar elliptical area that is vertical to the tethers. The individual systems are assigned non-overlapping flight cylinders depending on the wind direction. Detailed calculations that take into account Betz' limit, assuming a cubically averaged wind power density of 7 m/s, give a potential yearly average PD of 43 MW/km². A conventional wind farm with typical packing density would yield a PD of 2.4 MW/km² in the same wind field. More refined simulations using optimal control result in a more modest PD of 6.5 MW/km² for practically recommended flight trajectories. This PD can already be achieved with small-scale aircraft with a wing span of 5.5 m. The simulations additionally show that the achievable PD is more than an order of magnitude higher than for a single-aircraft AWE system with the same wing span.

© 2023 European Control Association. Published by Elsevier Ltd. All rights reserved.

1. Introduction

Because of the abundant availability of wind and solar energy resources, in principle only a tiny fraction of the earth's surface area would suffice to generate all of humanity's energy needs. Nevertheless the power density (PD) per ground surface area of wind and solar power technologies is still a relevant quantity. First, land availability close to urban regions with a high electricity demand is limited. In addition, the infrastructure costs of renewable energy farms, such as grid connection and installation logistics, scale proportionally with the farm area. The power density of existing wind power farms is estimated to be around PD = 2 MW/km². For solar PV farms we have a PD of around 10 MW/km² [14].

Airborne wind energy (AWE) is a renewable energy technology which aims at harvesting the steady and strong high-altitude winds that cannot be reached by conventional wind technology, at only a fraction of the resources. AWE developers mainly consider single-aircraft AWE systems (S-AWES), which are based on the principle of one tethered aircraft flying fast crosswind maneuvers. However, S-AWES are subject to several limitations that impede the technology to increase PD with respect to conventional wind.

First, S-AWES are characterized by high tether drag dissipation losses. These losses are inversely proportional to the aircraft size, which is why large and heavy (and thus, costly) aircraft are needed to achieve the efficiency needed for a high PD. Second, since the maximum tether length is limited due to the drag losses, S-AWES in farms would all operate at similar altitudes, leading to wake interaction between systems. Detailed wind field simulations of utility-scale S-AWES in farms suggest that these wake losses are comparable to those observed in conventional wind farms [7]. Therefore, a similar system spacing is required, resulting in ultimately the same achievable PD.

To overcome these limitations, this work proposes and simulates the concept of "vertical" AWE farms based on multi-aircraft AWE systems (M-AWES), as depicted in Fig 1. In M-AWES, previously investigated in [5,8,11,16] two or more aircraft fly very tight loops around a shared, quasi-stationary main tether. Because of the low tether drag, M-AWES are very efficient even for small aircraft size while using airspace more effectively, resulting in a lower trajectory footprint on the ground. The proposed vertical farm layout additionally exploits the fact that M-AWES can fly at arbitrarily high locations above the ground, so that they can operate at distinct locations in the sky, thereby avoiding wake interaction. A somewhat similar idea based on networked rotary AWE systems was proposed but not simulated in [13], with a focus on overall flight stability rather than power density.

* Corresponding author.

E-mail address: jochem.de.schutter@imtek.uni-freiburg.de (J. De Schutter).

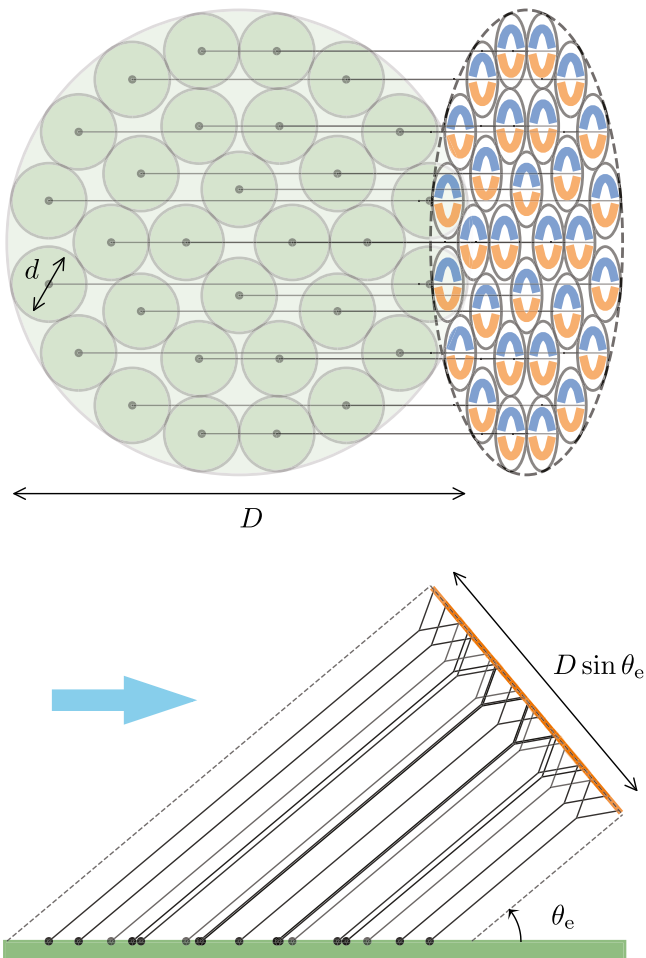


Fig. 1. Top and side view of a vertical M-AWES wind farm with $N = 30$, $\theta_e = 40^\circ$, $d/D = 0.16$ and $l_{\min}/D = 0.42$.

The remainder of this text is structured as follows. Section 2 describes the vertical farm concept and determines an upper PD limit based on a simplified analysis. Section 3 states the system model used in the simulation study while Section 4 proposes an optimal control problem (OCP) formulation to compute PD-optimal power cycles. Section 5 presents the numerical results of a case study, where we compute PD-optimal orbits for both S- and M-AWES, for a small and moderate aircraft size, and where we investigate the trade-off between PD and wing area efficiency. Section 6 discusses the main conclusions and gives suggestions for future research.

2. Vertical M-AWES farms

The vertical M-AWES farms proposed in this work are circular and consist of many independently ground located M-AWES that are all flying at the same tether inclination angle θ_e , but with different tether lengths, depending on the wind direction, such that all systems fly in a large planar elliptical area that is vertical to the tethers, as shown in Fig 1.

The individual systems are assigned non-overlapping “operation cylinders” that depend on the wind direction and correspond to a circular ground area. Otherwise, the individual systems are completely independent and can e.g. be started and landed independently. Each system might be located on a small tower in order to minimize its impact on the usability of the ground area, e.g. for agriculture.

The distance from one system to all others on the ground is lower bounded by the maximum diameter d of each systems ground area circle. The optimal circle packing density of N circles in a large circle of diameter D depends on N and is assumed to be $\rho_{\text{circle}} = 70\%$ here. Thus, from now on we assume that

$$N \frac{\pi d^2}{4} = \rho_{\text{circle}} \frac{\pi D^2}{4} \quad (1)$$

which means that we choose to build altogether $N = \rho_{\text{circle}} D^2/d^2$ individual units in the park. This abstracts from the individual systems size d and number N , such that we only need to remember the packing loss factor ρ_{circle} .

Together, the systems form a large inclined elliptical area in the sky. The area is perpendicular to the tethers, and thus forms an ellipse with a major axis width that is equal to D , but a minor axis width of $D \sin \theta_e$. The M-AWES are assumed to be able to fly ellipses with approximately this aspect ratio so the circle packing from the ground can be mapped by an affine transformation to the ellipse packing in the sky. The elliptical area forms an angle of θ_e with the vertical, and thus, the effective area of this “actuation ellipse” is again reduced by a factor $\cos \theta_e$ resulting in a height of the inclined ellipse of only $D \cos \theta_e \sin \theta_e$.

The shortest tether length l_{\min} defines the location of the lowest point of the ellipse, which is located $l_{\min} \sin \theta_e$ above the ground and $l_{\min} \cos \theta_e$ downwind, extending the ground boundaries of the wind park. This causes an extended park diameter $D + 2l_{\min} \cos \theta_e$, defining a circle above which the AWE systems can fly. This virtual area enlargement does not increase with park size, and since it does not lead to increased infrastructure costs, it can be neglected.

We assume that the M-AWES wing area is adapted to reach the Betz limit $\eta = 16/27$ on the available flight area assigned to each individual system. The overall power of the wind park is then proportional to its ground area, but affected by a variety of losses:

- the circle packing loss $\rho_{\text{circle}} = 70\%$;
- the geometric area reduction efficiency that reaches a maximum value of $\cos \bar{\theta}_e \sin \bar{\theta}_e = 0.5$ for $\bar{\theta}_e = 45^\circ$;
- the Betz factor $\eta = 16/27$;

leading altogether to an effective loss of

$$\eta_{\text{tot}} = \eta \cos \bar{\theta}_e \sin \bar{\theta}_e \rho_{\text{circle}} = 0.3 \rho_{\text{circle}} = 21\%. \quad (2)$$

The maximum power density is then given by

$$\text{PD}_{\text{max}} = \frac{1}{2} \eta_{\text{tot}} \rho_{\text{air}} v^3. \quad (3)$$

For example, for a cubically averaged wind speed of $v = 7$ m/s and $\rho_{\text{air}} = 1.2$ kg/m³ this results in a PD_{max} of 43 MW/km².

To obtain an estimate for a conventional wind energy farm operating in the same wind field, we assume operation at Betz’ limit and a circular packing with a distance of at least 6 rotor diameters between the systems. There are no geometric area reduction losses, resulting in a total efficiency $\eta_{\text{tot}} = 1.2\%$ and a PD_{max} of 2.4 MW/km² when wake losses are ignored. This PD is a factor 17 lower than the potential PD of the vertical M-AWES farm.

3. System model

To make a more realistic assessment, we will compute detailed, PD-optimal orbits for individual S- and M-AWES in this work. We consider “lift-mode” AWE systems, where power is produced in a periodic fashion: first, the tether is reeled out at high tension, driving a winch at the ground station. Then, tether is reeled back in again at low tension, resulting in a net positive energy gain. This section presents the M-AWES dynamics used in the optimal control problem formulation in Section 4 and introduces an averaged induction model to account for the Betz losses.

3.1. Multi-aircraft dynamics

In the following simulations, we use the multi-aircraft model structure and model parameters described in [5]. The system dynamics model all six degrees-of-freedom of the aircraft in the system. The tethers are assumed to be straight and inelastic, which is a good assumption when tether tension is high. The dynamics are expressed in non-minimal coordinates and summarized by the implicit index-1 DAE

$$F(\dot{x}(t), x(t), u(t), z(t), \theta, a) = 0 \quad (4)$$

and consistency conditions $C(x(t)) = 0$.

The system variables consist first of the state vector $x \in \mathbb{R}^{n_x}$. The control vector $u \in \mathbb{R}^{n_u}$ consists of the aircraft aileron, elevator and rudder deflection rates as well as the tether reeling acceleration. The algebraic state $z \in \mathbb{R}^{n_z}$ consists of the Lagrange multipliers related to the constraints that define the interlinkage of aircraft and tethers. The system parameters $\theta \in \mathbb{R}^{n_\theta}$ represent parameters that can be optimized over, such as the main tether diameter and, in the M-AWES case, the secondary tether length and diameter. The variable $a \in \mathbb{R}$ is the average induction factor that will be explained in Section 3.2.

For the sake of brevity, we refer the reader to [5] for a complete and formal description of the system variables, dynamics, aerodynamic forces, consistency conditions, etc. Here we only discuss those model components relevant for the wind power availability. We model the wind shear in a simplified way with a power law approximation:

$$u_\infty(z) = u_{\text{ref}} \left(\frac{z}{z_{\text{ref}}} \right)^{c_f}, \quad (5)$$

with $u_\infty(z)$ the freestream velocity at altitude z and u_{ref} the reference wind speed measured at altitude $z_{\text{ref}} = 100$ m, with $c_f = 0.15$ a surface friction coefficient typical for flat, open terrain.

The atmospheric density drop with altitude is modeled using the international standard atmosphere model [2]:

$$\rho(z) := \rho_0 \left(\frac{T_0 - T_L z}{T_0} \right)^{\frac{\kappa}{\gamma} - 1}, \quad (6)$$

where R is the universal gas constant. The parameters T_0 and ρ_0 are the temperature and air density at sea level, and T_L is the temperature lapse rate.

The model is based on a validated, small aircraft model with wing span $b_{\text{ref}} = 5.5$ m, mass $m_{\text{ref}} = 36.5$ kg and inertia tensor J_{ref} given in [12]. In order to be able to evaluate the dynamics also for larger wing spans b , we utilize the following mass upscaling formula:

$$m = m_{\text{ref}} \left(\frac{b}{b_{\text{ref}}} \right)^\kappa \quad \text{and} \quad J = J_{\text{ref}} \left(\frac{b}{b_{\text{ref}}} \right)^{\kappa+2}, \quad (7)$$

with upscaling exponent $\kappa = 2.4$.

3.2. Induction model

State-of-the-art induction models for AWE are typically a variation of Betz' analysis for conventional wind turbines, thus based on a steady-state analysis [3,10]. However, detailed wind field simulations [7] show that for lift-mode AWE systems, induction is inherently time-dependent: at the beginning of the reel-out phase, induction starts to build up, reaching its peak when transitioning into the reel-in phase, after which it starts to decline. When the power cycle re-starts, the wind is almost "fresh" again.

While the induction model proposed in [11] accounts for the dynamic variability of the aircraft trajectories over a power cycle, it still assumes an instantaneous build-up of induction. Therefore, in

this work, we propose the following model, based on a momentum balance applied to averaged flight quantities.

We first compute the annular swept area for each aircraft $k \in \mathcal{K}$, with \mathcal{K} the index set of all aircraft in the system. We integrate over the reel-out phase the norm of the aircraft's flight speed \dot{q} multiplied with the wing span, weighted with the local dynamic pressure:

$$A_{s,k} := \int_0^{T_{ro}} \frac{1}{2} \rho(q_{z,k}(t)) u_\infty^2(q_{z,k}(t)) b \|\dot{q}_k(t)\| dt, \quad (8)$$

where, by including the dynamic pressure inside the integral, we account for variability of wind speed and air density along the trajectory. The parameter T_{ro} is the reel-out phase duration, and $q_{z,k}$ is the vertical position component of aircraft k .

We assume that the force acting on this annulus is the main tether force, and that during the reel-in phase, this force is zero. The average tether force over one power cycle of period T is then given by:

$$\bar{F}_t := \frac{1}{T} \int_0^{T_{ro}} F_t(t) dt, \quad (9)$$

with the expression of the main tether force $F_t(t)$ in [5].

Momentum conservation applied to these average quantities then gives an algebraic equation for the average induction factor a , i.e.:

$$\bar{F}_t = 4a(1-a) \sum_{k \in \mathcal{K}} A_{s,k}.$$

The apparent wind speed that each aircraft k experiences is then given by

$$u_{a,k} := (1-a)u_\infty(q_{z,k})e_x - \dot{q}_k \quad (10)$$

with $e_x := [1 \ 0 \ 0]^T$ the unit vector in the x -direction.

Similar to the steady-state models proposed in [3] and [10], this induction model assumes that both flight annulus and tether force are perpendicular to the wind speed vector. This is a crude assumption, given that the main tether elevation angle is intrinsically non-zero. Nevertheless, this averaged approach gives a first-order account of the time-dependency of the induction for lift-mode systems, which is necessary in particular for lift-mode orbits with short reel-out phases.

By adding the values $A_{s,k}$ in the M-AWES case, we assume that the swept areas of the different aircraft do not overlap. To avoid double-counting, a no-overlap condition will be enforced as a constraint in the optimal control problem. For S-AWES, we will check a posteriori that the swept area does not self-overlap.

4. Problem formulation

This section discusses the path constraints used for the simulations in this work, and introduces a constraint which expresses the available flight cylinder as a function of the radius of the corresponding circular ground area. Then, this section presents a periodic OCP formulation to compute PD-optimal power cycles based on the dynamics presented in the previous section.

4.1. Flight envelope

Path constraints need to be enforced along the trajectory, to avoid flight envelope violations and to preserve structural integrity of the airframes and the tethers. More concretely, we impose the following constraints:

- Tether stress should not exceed the material yield stress with a safety factor 3.
- The tether force should be strictly positive to avoid tether sag and to preserve model validity.

- Aircraft roll and pitch angles should be smaller than 90° to avoid collision with the tether.
- The angle-of-attack and side-slip angle of all aircraft are bounded to avoid stall and preserve model validity.
- The aileron, elevator and rudder control surfaces and their rates are bounded.
- The aircraft should remain above the ground with a safety distance of 100 m.
- The tether length is bounded from above by a value $l_{t,max} = 700$ m.
- The induction factor a should be positive and smaller than 0.5 to avoid flow acceleration or reversal.

We refer the reader to [5] for those numerical bound values not mentioned explicitly in this text.

4.2. Cylindrical flight constraint

A central feature of vertical M-AWES farms is that each system is assigned an individual, tilted flight cylinder. The intersection of this flight cylinder with the ground gives a circular area with radius R ($= d/2$). The flight cylinder has an ellipsoidal cross-section with a major axis length R and a minor axis length $R \sin \theta_e$, with θ_e the elevation angle of the cylinder. This elevation angle is included as an optimization variable.

We express the flight cylinder constraint for all aircraft in the system in the following way. Note that for M-AWES, the constraint is also imposed on the juncture node between main tether and secondary tethers. First, we rotate the aircraft position into the ellipsoidal cylinder frame:

$$\hat{q}_{y,k} := q_{y,k} \quad (11)$$

$$\hat{q}_{z,k} := q_{z,k} \cos(\theta_e) - q_{x,k} \sin(\theta_e). \quad (12)$$

Then, we define the constraining ellipse axes as

$$\hat{R}_y := R - b/2 \quad (13)$$

$$\hat{R}_z := R \sin \theta_e - b/2, \quad (14)$$

which ensures that the entire wing with span b remains in the ellipse. The constraint then reads as

$$\frac{\hat{q}_{z,k}^2}{\hat{R}_z^2} + \frac{\hat{q}_{y,k}^2}{\hat{R}_y^2} \leq 1. \quad (15)$$

These flight constraints, together with the constraints mentioned in Section 4.1 are summarized by the expression $h(x(t), u(t), z(t), \theta, a, R, \theta_e) \geq 0$.

In the M-AWES case, we need to ensure that the swept areas of the two connected aircraft do not overlap during the reel-out phase in order to avoid double-counting. For the purposes of this work, we therefore propose to pre-structure the M-AWES OCP so that the solution consists of one single loop: half a loop for the reel-out phase, and half a loop for the reel-in phase. During the reel-out phase, each aircraft is assigned one half of the flight cylinder. During the reel-in phase, the two aircraft switch flight regions.

Formally, we express the no-overlap constraint for aircraft k as

$$h_{no,k}(x, \theta_e, \phi_0) := \hat{q}_{z,k} \cos(\phi_0) - \hat{q}_{y,k} \sin(\phi_0). \quad (16)$$

The angle ϕ_0 rotates the intersecting half-plane that divides the flight cylinder in two and can be chosen freely by the optimizer.

For a dual-aircraft system, with aircraft nodes $k \in \mathcal{K} = \{2, 3\}$, the no-overlap condition for the two aircraft is combined with a phase-fixing constraint on the tether reel-out speed \dot{l}_t :

$$h_{no}(x, \theta_e, \phi_0) := \begin{bmatrix} h_{no,2}(x, \theta_e, \phi_0) \\ -h_{no,3}(x, \theta_e, \phi_0) \\ \dot{l}_t \end{bmatrix}. \quad (17)$$

Table 1

PD-optimal (A-D) and practically recommended (E) solution parameters and outputs.

Label	System	b [m]	a [-]	R [m]	PD [$\frac{MW}{km^2}$]	\bar{P} [kW]
A	S-AWES	5.5	0.01	44.0	0.2	1.9
B	M-AWES	5.5	0.21	15.4	8.4	8.9
C	S-AWES	26.0	0.05	103.4	2.1	100.0
D	M-AWES	26.0	0.10	81.9	10.2	308.0
E	M-AWES	5.5	0.13	28.5	6.5	23.7

This constraint is greater or smaller than zero depending on the phase.

4.3. Optimal control problem

We can now directly compute periodic flight trajectories that optimize the power density, by solving the following periodic OCP:

$$\begin{aligned} \min_{\substack{x(\cdot), u(\cdot), z(\cdot) \\ \theta, a, T_{ro}, T_{ri} \\ R, \theta_e, \phi_0}} & -\frac{1}{T} \int_0^T \rho_{circle} \frac{P(t)}{\pi R^2} dt \\ \text{s.t.} & F(\dot{x}(t), x(t), u(t), z(t), \theta) = 0, \forall t \in [0, T], \\ & h(x(t), u(t), z(t), \theta, a, R, \theta_e) \geq 0, \forall t \in [0, T], \\ & h_{no}(x(t), \theta_e, \phi_0) \geq 0, \forall t \in [0, T_{ro}], \\ & -h_{no}(x(t), \theta_e, \phi_0) \geq 0, \forall t \in (T_{ro}, T], \\ & x(0) - x(T) = 0, \\ & \bar{F}_t - 4a(1-a) \sum_{k \in \mathcal{K}} A_{s,k} = 0, \end{aligned}$$

where the overall time T is defined as the sum of the reel-out time and the reel-in time, which are free optimization variables: $T := T_{ro} + T_{ri}$. The initial and final state of the trajectory are free, but must be equal. The cost function is chosen so as to maximize the average power output divided by the circular ground area occupied by the system. This PD is multiplied with ρ_{circle} to account for packing losses.

The M-AWES OCP is discretized using direct collocation with 40 intervals, and Radau polynomials of degree 4. For S-AWES, the no-overlap conditions in (17) are omitted, but the phase-fixing constraint is retained. Since the optimal time period is larger for this problem, we increase the number of collocation intervals to 100.

The NLP is formulated in Python using the open-source AWE optimal control framework AWEbox [4], which builds on the symbolic framework for algorithmic differentiation and nonlinear optimization CasADi [1]. AWEbox solves the NLP with IPOPT [15] and the linear solver MA57 [9].

5. Numerical results

This section presents and discusses PD-optimal periodic orbits for M-AWES and S-AWES, both for a small and moderate aircraft size. In a second step, periodic orbits for each variant are computed for a range of fixed values for the ground circle radius R , in order to investigate the trade-off between power density and wing area efficiency. We conclude with a critical discussion of the obtained results in the light of the modeling assumptions.

5.1. Optimal power density solutions

The periodic OCP is solved for both a S-AWES and a M-AWES with two aircraft. First we use the small wing span ($b = 5.5$ m) of the original aircraft model. Then we do the same for an up-scaled version of the same model ($b = 26$ m). Table 1 summarizes

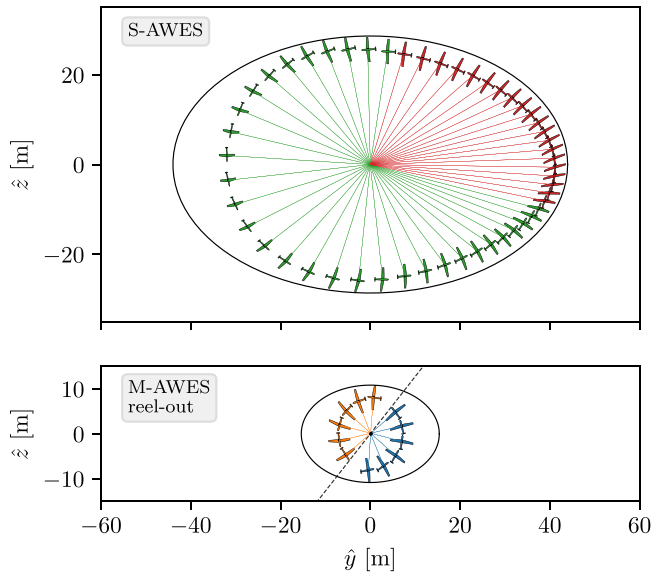


Fig. 2. PD-optimal flight trajectories in ellipsoidal coordinates for $b = 5.5$ m, with $\theta_c^* \approx 44^\circ$. For the S-AWES trajectory, the aircraft is colored green in the reel-out phase, and red in the reel-in phase. For clarity of presentation, only the reel-out phase of the M-AWES trajectory is plotted. (For interpretation of the references to colour in this figure legend, the reader is referred to the web version of this article.)

the optimal results for the different variants. All of the results have a similar optimal elevation angle $\theta_c^* \approx 44^\circ$. This is close to the theoretically optimal value of 45° obtained in Section 2.

Fig. 2 shows the optimal trajectories for the small-size S-AWES and M-AWES. The S-AWES has a rather large optimal ground circle radius $R^* = 44.0$ m, and very low power output because of the large tether drag losses. Hence the power density is also impractically low (0.2 MW/km²). The optimal radius for the M-AWES is a factor 3 smaller, at a value less than three wing spans. The dual-aircraft configuration thus allows the system to fly extremely tight circles. Combined with the efficiency gain due to reduced tether drag and the increased flying altitude, this results in a power density that is 38 times higher (8.4 MW/km²) than for S-AWES. Optimizing for power density drives this system to make very efficient use of the available airspace: the optimal induction factor $a^* = 0.21$ is close to the theoretically optimal value of $1/3$. For the S-AWES, induction is almost negligible.

Fig. 3 shows the optimal trajectories for the moderate-size S-AWES and M-AWES. The S-AWES solution improves on two fronts compared to the small-size results. First, since the relative tether

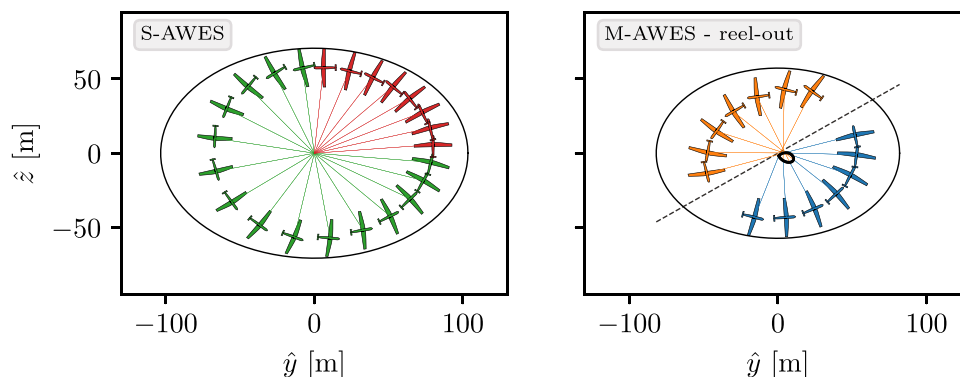


Fig. 3. PD-optimal flight trajectories in ellipsoidal coordinates for $b = 26.0$ m, with $\theta_c^* \approx 44^\circ$. For the S-AWES trajectory, the aircraft is colored green in the reel-out phase, and red in the reel-in phase. For clarity of presentation, only the reel-out phase of the M-AWES trajectory is plotted. (For interpretation of the references to colour in this figure legend, the reader is referred to the web version of this article.)

drag contribution to the total system drag decreases with increasing aircraft size, the moderate-size system is more efficient and flies at a higher altitude, resulting in a significantly higher power output. Second, for a more than four times larger aircraft, the ground area radius only increases by a factor of 2.4, the induction factor increases by a factor of 5, and the PD (2.1 MW/km²) increases by a factor larger than 9. Note that this PD is similar to that of conventional wind.

For the M-AWES, the ground radius increases with a factor of 5, but the large aircraft size also reduces the impact of the secondary tether drag, which is why the power density increases slightly to 10.2 MW/km², which is still almost a factor of 5 larger than for the moderate-size S-AWES.

It should be noted that while in the envisioned vertical wind farms, M-AWES need an individual flight cylinder to avoid collisions, this need not be the case for S-AWES. In fact, S-AWES can be packed closer together than done in this work, e.g. with overlapping flight cylinders when synchronized properly, as proposed in [6]. Such a strategy could ultimately improve the PD of S-AWES.

On the other hand, the obtained PD for the moderate-scale S-AWES is also too optimistic. Either the systems operate in a “horizontal” configuration, i.e. each system in its own cylinder but at the same tether length and thus at an identical flying height. In this case, additional wake losses need to be taken into account. These losses increase as systems grow larger and are packed more closely together. Or the systems operate “vertically” with different tether lengths, avoiding wake interaction. In this case, additional drag losses for the systems with longer tethers need to be considered. In this sense, the obtained PD for S-AWES is not overly pessimistic.

5.2. Trade-off between ground and wing area

Optimizing for power density results in a suboptimal solution in terms of average power output for a given wing area $\bar{P}_S := \bar{P}/(|\mathcal{K}|S)$, with S the aerodynamic surface of a single aircraft in the system. In practice, a trade-off between these two objectives needs to be found: for a given power output, we want to both minimize the trajectory footprint and the required wing area.

Starting from the PD-optimal solution, the Pareto front between PD and \bar{P}_S is constructed by re-solving the OCP for fixed and increasing values of R . Fig. 4 shows the result of this parametric sweep for all variants. After a certain value of R , the \bar{P}_S -optimal solution is reached and the cylindrical flight constraint becomes inactive for all larger R .

For increasing R , all system variants are able to increase power output in two ways. First, the systems fly at lower, more power-optimal elevation angles, down to a value $\theta_c \approx 24^\circ$ for all variants.

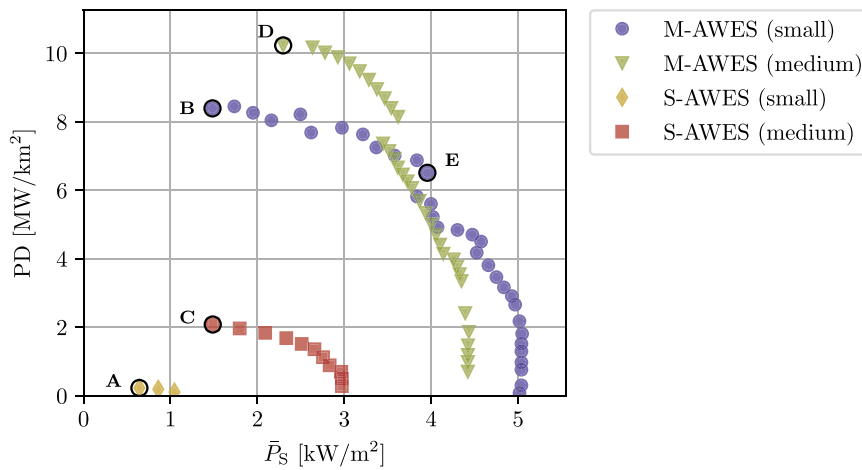


Fig. 4. Pareto efficiency front between power density and power per wing area for small- and medium-size S-AWES and M-AWES.

The larger value of R compensates the minor ellipse axis reduction with $\sin \theta_e$. Second, the systems fly trajectories with a larger harvesting area, which results in a lower induction factor but overall in a net increase in power.

The M-AWES power output per wing area increases by a factor over 3 for the small-size system and a factor of 2 for the moderate-size system, at the cost of reducing the PD with a factor of 3 in both cases. A good compromise for the small-size system might be $PD \approx 6.5 \text{ MW/km}^2$ and $\bar{P}_S \approx 4 \text{ kW/m}^2$, marked by the label “E” in Fig. 4 and summarized in Table 1. Interestingly, the small-size M-AWES completely dominates the moderate-size S-AWES by a large margin. M-AWES based on small aircraft can thus be efficiently deployed both as a single unit for small-scale applications, as well as in AWE farms for utility-scale electricity generation.

6. Conclusion

In this paper we proposed vertical M-AWES farms with high PD per ground area. We determined the theoretical potential of these farms and computed and compared detailed PD-optimal flight trajectories for both M-AWES and S-AWES of different sizes. The achieved PD of the recommended small-size M-AWES design “E” is significantly lower than the theoretical estimate, by a factor of 6.6. A big loss factor is the fact that the optimal flight annulus only covers part of the elliptical cross-section, and thus does not exploit the total available harvesting area. Future work should explore M-AWES trajectories that use more area of the elliptical cylinders in order to achieve power densities that are closer to what is theoretically possible.

Declaration of Competing Interest

The authors declare that they have no known competing financial interests or personal relationships that could have appeared to influence the work reported in this paper.

Acknowledgements

This research was supported by DFG via Research Unit FOR 2401 and project 424,107,692 and by the EU via ELO-X 953348.

References

- [1] J.A.E. Andersson, J. Gillis, G. Horn, J.B. Rawlings, M. Diehl, CasADi – a software framework for nonlinear optimization and optimal control, *Mathematical Programming Computation* 11 (1) (2019) 1–36, doi:10.1007/s12532-018-0139-4.
- [2] C. Archer, *An introduction to meteorology for airborne wind energy*, in: *Airborne Wind Energy*, Springer Berlin / Heidelberg, 2013.
- [3] M. De Lellis, R. Reginatto, R. Saraiva, A. Trofino, The betz limit applied to airborne wind energy, *Renewable Energy* 127 (2018) 32–40.
- [4] J. De Schutter, R. Leuthold, T. Bronnenmeyer, E. Malz, S. Gros, M. Diehl, Awe-box: An optimal control framework for single- and multi-aircraft airborne wind energy systems, *Energies* 16 (4) (2023) 1900, doi:10.3390/en16041900.
- [5] J. De Schutter, R. Leuthold, T. Bronnenmeyer, R. Paelinck, M. Diehl, Optimal control of stacked multi-kite systems for utility-scale airborne wind energy, in: *Proceedings of the IEEE Conference on Decision and Control (CDC)*, 2019, doi:10.1109/CDC40024.2019.9030026.
- [6] P. Faggiani, R. Schmehl, *Airborne Wind Energy: Advances in Technology Development and Research*, Springer Singapore, 2018, pp. 391–411.
- [7] T. Haas, J. De Schutter, M. Diehl, J. Meyers, Large-eddy simulation of airborne wind energy farms, *Wind Energy Science* 7 (3) (2022) 1093–1135.
- [8] B. Houska, M. Diehl, Optimal control for power generating kites, in: *Proceedings of the European Control Conference (ECC)*, 2007, pp. 3560–3567. Kos, Greece.
- [9] HSL, A collection of Fortran codes for large scale scientific computation., 2011, <http://www.hsl.rl.ac.uk>.
- [10] M. Kheiri, V.S. Nasrabad, F. Bourgault, A new perspective on the aerodynamic performance and power limit of crosswind kite systems, *Journal of Wind Engineering and Industrial Aerodynamics* (2019).
- [11] R. Leuthold, J. De Schutter, E.C. Malz, G. Licitra, S. Gros, M. Diehl, Operational regions of a multi-kite awe system, in: *European Control Conference (ECC)*, 2018, doi:10.23919/ECC.2018.8550199.
- [12] E.C. Malz, J. Koemann, S. Sieberling, S. Gros, A reference model for airborne wind energy systems for optimization and control, *Renewable Energy* 140 (2019) 1004–1011.
- [13] R. Read, Kite networks for harvesting wind energy, in: *Airborne Wind Energy: Advances in Technology Development and Research*, Springer Singapore, 2018.
- [14] J. Van Zalk, P. Behrens, The spatial extent of renewable and non-renewable power generation: A review and meta-analysis of power densities and their application in the u.s., *Energy Policy* 123 (2018) 83–91.
- [15] A. Wächter, L.T. Biegler, On the implementation of an interior-point filter line-search algorithm for large-scale nonlinear programming, *Mathematical Programming* 106 (1) (2006) 25–57.
- [16] M. Zanon, S. Gros, J. Andersson, M. Diehl, Airborne wind energy based on dual airfoils, *IEEE Transactions on Control Systems Technology* 21 (2013) 1215–1222, doi:10.1109/TCST.2013.2257781.